SI Appendix

Methods

Animals

Wild-type C57BL/6 mice were kept under 12 h light / 12 h dark cycle with *ad libitum* access to food and water (strain from Jackson Labs, Bar Harbor, ME).

Viral infection

For specifically labelling CA3 neurons, a glass micropipette backfilled with Sindbis-GFP viral particles diluted in TNE buffer containing (in M) 0.1 NaCl, 0.05 Tris-Cl (pH 8), 0.5 EDTA, and 0.001% Tween-20, connected to a pressure-injection device (Picospritzer, Parker, Hollis, NH, USA) was used. The pipette was positioned into CA3 pyramidal layer and the virus was injected by brief pressure pulses (50-150 ms; 10-15 psi) yielding an infection of approximately 30-50 neurons. Experiments were conducted 36-48 h after the infection giving sufficient GFP expression, while preserving the physiological health of the cells.

Recording solutions

For the imaging experiments, slice cultures were transferred into a heated recording chamber at 32°C and continuously perfused with carbogenated (95% O_2, 5% CO_2) artificial cerebrospinal fluid (ACSF) at pH 7.4 with an osmolarity of 300-310 mOsm containing (in mM) 124 NaCl, 3 KCl, 2 $CaCl_2$, 1 $MgCl_2$, 10 glucose, 1.25 NaH_2PO_4, 26 $NaHCO_3$, 2.5 sodium L-ascorbate, 2 trolox (Sigma-Aldrich, St. Louis, MO, USA). Specified experiments were performed in the presence of 50 µM D-APV (Tocris Bio-Techne, Lille, France), 10 µM NBQX (2,3-dihydroxy-6-nitro-7-sulfamoyl-benzo[f]quinoxaline-2,3-dione; Tocris Bio-Techne, Lille, France), 2 mM kynurenate (Sigma-Aldrich, St. Louis, MO, USA) or 100 µM of cadmium ($CdCl_2$, Sigma-Aldrich, St. Louis, MO, USA).

For studying the morphological changes in a single cell approach, hippocampal CA3 pyramidal neuron were patch-loaded using glass capillaries (tip resistance 5-8 MΩ) containing 600 µM Atto488 (ATTO-tec, Siegen, Germany) and the following (in mM): 125 K-gluconate, 5 KCl, 10 HEPES, 1 EGTA, 4 Mg-ATP, 0.3 Na-GTP, 10 Na-phosphocreatine and 3 ascorbic acid (pH=7.3). CA3 pyramidal neurons were recorded in current clamp mode with a dynamic current injection correction to maintain the resting membrane at -70 mV.

Myelin immunostaining

Hippocampal slice cultures infected with Sindbis-GFP viral particles in the CA3 pyramidal layer were fixed 36-48h after the infection overnight in 4% paraformaldehyde (PFA, VWR, Pennsylvania, USA) at 4°C. After washing in phosphate buffer (0.1M PB), slices were removed from their coverslips to be processed as free-floating slices for immunostaining. Briefly, permeabilization and blocking was realized by incubation of the free-floating sections for 24h at 4°C in 0.1M PB, 0.4% Triton X-100 and 10% Normal goat serum (NGS, Vector Laboratories, Burlingame, USA). The sections were then incubated with the polyclonal rabbit anti-Myelin Basic Protein (MBP) antibody (1:1000, Abcam, Cambridge, MA, USA) overnight at 4°C in 0.1M PB, 0.4% Triton X-100 and 5% NGS. Following washing, the sections were incubated with the Alexa 568-conjugated goat anti-rabbit secondary antibody (1:400, Invitrogen, USA) overnight at 4°C.

For fixed brain slices, 1 month old mice were sacrificed with a lethal dose of sodium pentobarbital (200 mg/kg, i.p., Centravet, Dinan, France) and perfused transcardially with a saline solution followed by 4% PFA in 0.1M PB. Brains were removed, post-fixed in 4% PFA for 6-8 hours, and then sectioned in the coronal plane on a vibratome at 40µm. The slices were blocked and permeabilized with a blocking buffer containing 5% NGS and 0.5% Triton X-100 for 1h at room temperature. Then they were incubated with the rabbit anti-MBP antibody (1:1000, Abcam, Cambridge, MA, USA) overnight at 4°C and visualized using the Alexa 568-conjugated goat anti-rabbit secondary antibody (1:500, Invitrogen, CA, USA).

Slice cultures were mounted in Mowiol (Millipore, Darmstadt, Germany) and fixed brain slices in an antifade mounting medium containing DAPI (Vectashield, Vector laboratories, Burlingame, USA) for imaging. Images were acquired using a commercial inverted confocal microscope (Leica DMI6000 TCS SP8 X, Leica Microsystems, Mannheim, Germany). Large field of views were acquired with a 10X HC Plan Fluotar objective (NA 0.3, dry) with a pixel size of ~300nm at a scan speed of 400 Hz using 6 line averages or with a HC Plan Apo CS2 20X multi-immersion objective (NA 0.75) with a pixel size of ~200nm at a scan speed of 400Hz using 8 line averages. High resolution images of CA3 and CA1 *stratum radiatum* were acquired using a HCX Plan Apo CS2 63X oil objective (NA 1.40) with a pixel size of ~70 nm and a z-step size of 400 nm and at a scan speed of 400 Hz using 4 line averages.

For MBP immunostaining, maximal intensity projection (MIP) images of 4 µm thickness image stacks of the GFP labelling were used to determine the total length of axons in the field of view. The length measurement was obtained by thresholding and binarizing the MIP images before using a skeletonization plugin from ImageJ. The length of myelinated axons were measured with the NeuronJ plugin on MIP images of the MBP labelling and confirmed by stepping through the 3D stacks of merged images. Image stacks were taken in 3 slices from 2 different cultures. In each slice, 4 image stacks in the *stratum radiatum* of CA3 and 3 image stacks in the *stratum radiatum* of CA1 were analysed. About 20 mm of axon length was measured per slice.

Single-cell axon imaging

After 5 min of patch-loading, fluorescently labelled axon from a CA3 pyramidal cell was tacked from the soma to one of the first branch, where we choose our region of interest. Exposure time was minimized to avoid phototoxic damage.

For the HFS protocol, confocal image stacks were acquired with a voxel size of 39 × 39 × 375 (x, y, z, in nm) and pixel dwell time of 15 µs. Confocal images were acquired at −5, 1, 21 min relative to HFS induction. The stimulus protocol consisted of 3 trains of 100 pulses (5 ms, 1.3 to 2.3 nA) delivered at 100 Hz and 20 seconds apart. As some current pulses failed to elicit an AP, experiments were sorted and selected according to the total number of APs generated at the soma. When ≥200 APs were elicited out of 300 current pulses, the HFS was considered successful. In specified experiments using cadmium, the drug was applied 10 min before the stimulation and washed out 5 min afterwards.

For the TBS protocol, STED image stacks were acquired with a voxel size of 25 × 25 × 375 (x, y, z, in nm) and dwell time of 10 µs. To improve imaging depth penetration, we used a glycerine objective, which is equipped with a correction collar to reduce spherical aberrations. STED images were acquired at −5, 1, 45 min relative to TBS induction. The stimulus protocol consisted of a series of ten short 100 Hz pulse trains (3 in total and 20 seconds apart), of five pulses each

spaced by 9 ms (1 ms, 1.5 to 3.5 nA, inter-burst interval of 150 ms), delivered at a frequency of 5 Hz.

Calcium imaging

For bulk loading of CA3 pyamidal neurons in brain slices, the calcium-sensitive Oregon Green BAPTA-1 acetylomethyl ester (OGB-1 AM, Molecular Probes, Eugene, OR, USA) was first dissolved in 4 µl DMSO containing Pluronic F-127 (Molecular Probes), and then diluted (1/11) in ACSF resulting in a final concentration of 0.9 mM. A glass micropipette backfilled with this solution, connected to a pressure-injection device (Picospritzer, Parker, Hollis, NH, USA) was used. The pipette was positioned into CA3 pyramidal layer and the solution was injected by brief pressure pulses (50-150 ms; 10-15 psi). Slices were incubated 30 min to 1 hour prior imaging. We used the same electrical field stimulation that was used in the structural imaging experiments and recorded calcium transients in several axons segment by confocal imaging at a frame rate of 5.9 Hz.

Bouton turnover analysis

The one-hour long time-lapse experiments were analysed to determine the turnover of boutons. For each axon segment and each time point, the presence of boutons was determined based on their diameter profile generated by a custom-written Matlab script. Boutons were defined as stable when they were present at all time points. A gained/lost bouton was defined as a bouton that appeared/disappeared in at least one of the time points.

Numerical simulations

-Geometry of model axon

The simulation model consisted of 4 sections: to give the model a realistic behavior (i.e. in order to avoid sealed effects from interfering with the analysis), the *simulated branch (3)* was included after a 500 µm *proximal axon (2)* (used to simulate realistic incoming spike), and before a *distal axon (4)* of 200 µm in which spikes propagate after traveling in the simulated branch. Spikes were initiated in an *initial segment (1*) (by current pulse injection in the soma) before accessing the 500 µm axon. In each section, the number of segments was an odd number calculated according to the d-lambda rule. The frequency of 1 kHz was chosen because simulated fast spikes are in this frequency domain. The value of d-lambda was adjusted by progressively decreasing it (starting from 0.1) until further change did not result in any measurable change in spike velocity.

The temporal integration step was 25 µs. The tested sequences consisted of a mirrored repetition of diameter profiles obtained after automated analysis of axon segments acquired in STED mode and normalized to a length of 500 nm in order to avoid edge effects.

-Passive electrical properties

The intra-compartmental potential, E, is described by the differential equation

$$\frac{dE}{dt} = \frac{I_{leak} + I_{core} + I_{ch}}{c_m} \quad (1)$$

where I_{leak} is the passive leakage current

$$I_{leak} = (E_{leak} - E) \times G_{leak} \quad (2)$$

and E_{leak} and G_{leak} are the equilibrium potential and the leak conductance, respectively.

I_{core} is the axial current to neighboring compartments summed over all neighbors

$$I_{core} = \sum_{c \in neighbors} (E_c - E) \times G_{core} \quad (3)$$

The parameter G_{core} (in S) denotes the core conductance from the compartment in question to the neighboring compartment:

$$G_{core} = \frac{\pi \times diam^2}{4} \times \frac{1}{l} \times \frac{1}{R_a} \quad (4)$$

where *diam* and *l* are diameter and length of the compartment (in cm), respectively ; R_a is the specific resistance of the axoplasm (in Ω·cm).

I_{ch} in equation (1) is intrinsic currents. Intracellular current injection can be modeled by adding current to the compartment. The parameter c_m (µF) describes the capacitance of the compartment

$$c_m = C_m \times area \quad (5)$$

(*area* is the membrane surface of the compartment in cm^2, C_m is the specific capacitance in $\mu F \cdot cm^{-2}$)

All compartments had the same specific membrane resistance (R_m) set to 10000 $\Omega \cdot cm^2$. All computations were carried out assuming a specific capacitance, C_m of $1 \mu F/cm^2$ and a specific axoplasmic resistance, R_a, of 100 Ω·cm.

-Sodium and potassium channels

Sodium (Na^+) current is computed as

$$I_{Na} = (E_{Na} - E) \times G_{Na} \times m^3 \times h \quad (6)$$

The activation variable *m* is described by

$$\frac{dm}{dt} = \alpha_m \times (1 - m) - \beta_m \times m \quad (7)$$

with rate functions α_m and β_m

$$\alpha_m = \frac{A_{\alpha_m} \times k_{\alpha_m} \times (E - d_{\alpha_m})}{1 - e^{-k_{\alpha_m} \times (E - d_{\alpha_m})}} \quad (8)$$

$$\beta_m = \frac{A_{\beta_m} \times k_{\beta_m} \times (E - d_{\beta_m})}{1 - e^{-k_{\beta_m} \times (E - d_{\beta_m})}} \quad (9)$$

The inactivation variable *h* is computed in a similar way.

$$\frac{dh}{dt} = \alpha_h \times (1 - h) - \beta_h \times h \quad (10)$$

With rate functions α_h and β_h

$$\alpha_h = A_{\alpha_h} \times e^{k_{\alpha_h} \times (E - d_{\alpha_h})} \quad (11)$$

$$\beta_h = \frac{A_{\beta_h}}{1 + e^{k_{\beta_h} \times (E - d_{\beta_h})}} \quad (12)$$

In most computations, we used the following values for the Na^+ channel parameters (IS):

Activation *m*:

$$A_{\alpha m} = 1.28\, ms^{-1}\,;\, k_{\alpha m} = 0.25\, mV^{-1};\, d_{\alpha m} = -42\, mV \quad (13)$$

$$A_{\beta m} = 1.4\, ms^{-1};\, k_{\beta m} = -0.2\, mV^{-1};\, d_{\beta m} = -15\, mV \quad (14)$$

Inactivation *h*:

$$A_{\alpha h} = 0.128\, ms^{-1};\, k_{\alpha h} = -0.0555\, mV^{-1};\, d_{\alpha h} = -38\, mV \quad (15)$$

$$A_{\beta h} = 4\, ms^{-1};\, k_{\beta h} = -0.2\, mV^{-1};\, d_{\beta h} = -15\, mV \quad (16)$$

The maximum conductance density for Na^+ channels in a given compartment was G_{Na} Max = 0.24 S·cm^{-2} in the initial segment, and G_{Na} Max = 0.06 S·cm^{-2} in other sections of the model. The equilibrium potential for Na^+ ions was set E_{Na} = +50 mV.

Potassium (K^+) current is computed as:

$$I_k = (E_k - E) \times G_k \times n^4 \quad (17)$$

Its activation variable, n, is described by the equation:

$$\frac{dn}{dt} = \alpha_n \times (1 - n) - \beta_n \times n \quad (18)$$

with rate functions α_n and β_n

$$\alpha_n = \frac{A_{\alpha_n} \times k_{\alpha_n} \times (E - d_{\alpha_n})}{1 - e^{-k_{\alpha_n} \times (E - d_{\alpha_n})}} \quad (19)$$

$$\beta_n = A_{\beta_n} \times e^{k_{\beta_n} \times (E - d_{\beta_n})} \quad (20)$$

In all computations, we used the following values for the K^+ channel parameters:

$$A_{\alpha n} = 0.16\, ms^{-1};\, k_{\alpha n} = 0.2\, mV^{-1};\, d_{\alpha n} = -40\, mV \quad (21)$$

$$A_{\beta n} = 0.5\, ms^{-1};\, k_{\beta n} = -0.025\, mV^{-1};\, d_{\beta n} = -45\, mV \quad (22)$$

The maximum conductance density was G_{KMax} = 0.048 S.cm^{-2} in the initial segment, and 0.08 S.cm^{-2} in the other sections of the model. The equilibrium potential for K^+ ions was E_K = -77 mV.

Statistics

Data are presented as median values with interquartile range or as mean with s.e.m., s.d., or the 95% confidence interval (95% CI) as specified. Statistical comparisons and parameters of variability are specified under Results. Two sample t-tests comparing 30-40 min after HFS and before were used for the fEPSP recordings. Kruskal-Wallis test used to assess the stability of the structural parameters. For the structural plasticity experiments, skewness of data ranged between, -0.5 and 2.7. One-way repeated ANOVA were performed to test the structural changes over time. Post-hoc Dunnett test was performed to determine the significantly different time points from the baseline. One-sample t-test was used for the comparison of coefficients of variation. For the latency measurements, normality of data distribution was tested by D'Agostino and Pearson normality test. One-tailed paired t-test was used to test whether latency increased right after stimulation and decreased later. One-sample Wilcoxon test was used to compare the number of APs vs the magnitude of bouton size increase. All data are displayed as mean ± s.e.m. n.s., not significant; *P < 0.05; **P < 0.01; ***P < 0.001.

Figures

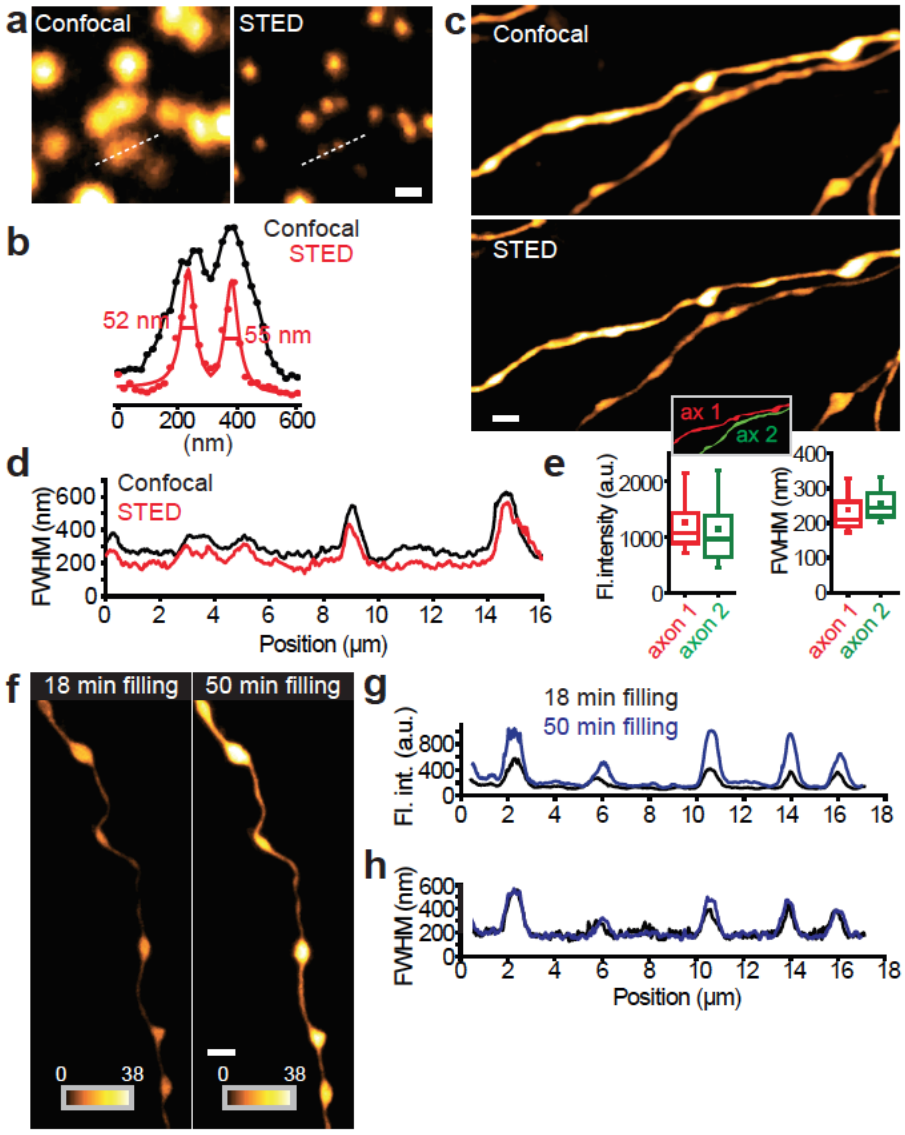

Fig. S1. Validation of resolution gain of STED over confocal microscopy

a, Imaging 40 nm fluorescent beads reveals a substantial gain in spatial resolution by STED over confocal microscopy. The two images were produced sequentially – first, the Gaussian excitation beam was scanned across the field of view to image the beads (confocal) and rescanned adding the 'doughnut' depletion beam (STED). **b**, Intensity profiles corresponding to the dotted lines in the images are depicted in the graph (raw data, dots). The FWHM from Lorentzian fits on the STED intensity profiles (red line) illustrates the gain in resolution whereas in confocal mode it was not possible to discriminate the two beads (black line). **c**, Resolution improvement on GFP-labelled CA3 axons. **d**, Comparison between the FWHM profiles of axon 1 in confocal vs. STED shows that STED is able to capture the morphology of the axon well below the limit of optical resolution. **e**, Graphs showing that the average intensity is not a reliable reporter of axon diameter. While axon 1 is brighter than axon 2, its average diameter is smaller. **f-h**, The level of filling the neuron with Atto 488 did not affect the FWHM measurements. **f**, Same axon segment imaged after 18 and 50 min of filling with Atto 488 show the increase of signal intensity correlating with increase of dye concentration. **g**, Plot of fluorescence intensity integrated over the width of the axon ('area under the curve') shown in (f) as a function of axon length. Any estimate of axon diameter based on the level of absolute fluorescence will be sensitive to differences or changes in dye concentration due to loading, bleaching or intracellular volume displacement. **h**, By contrast, the FWHM is a measure of axon diameter, which is insensitive to such variations, in particular differences in dye filling. Scale bars, 200 nm (a), 1 µm (c and f).

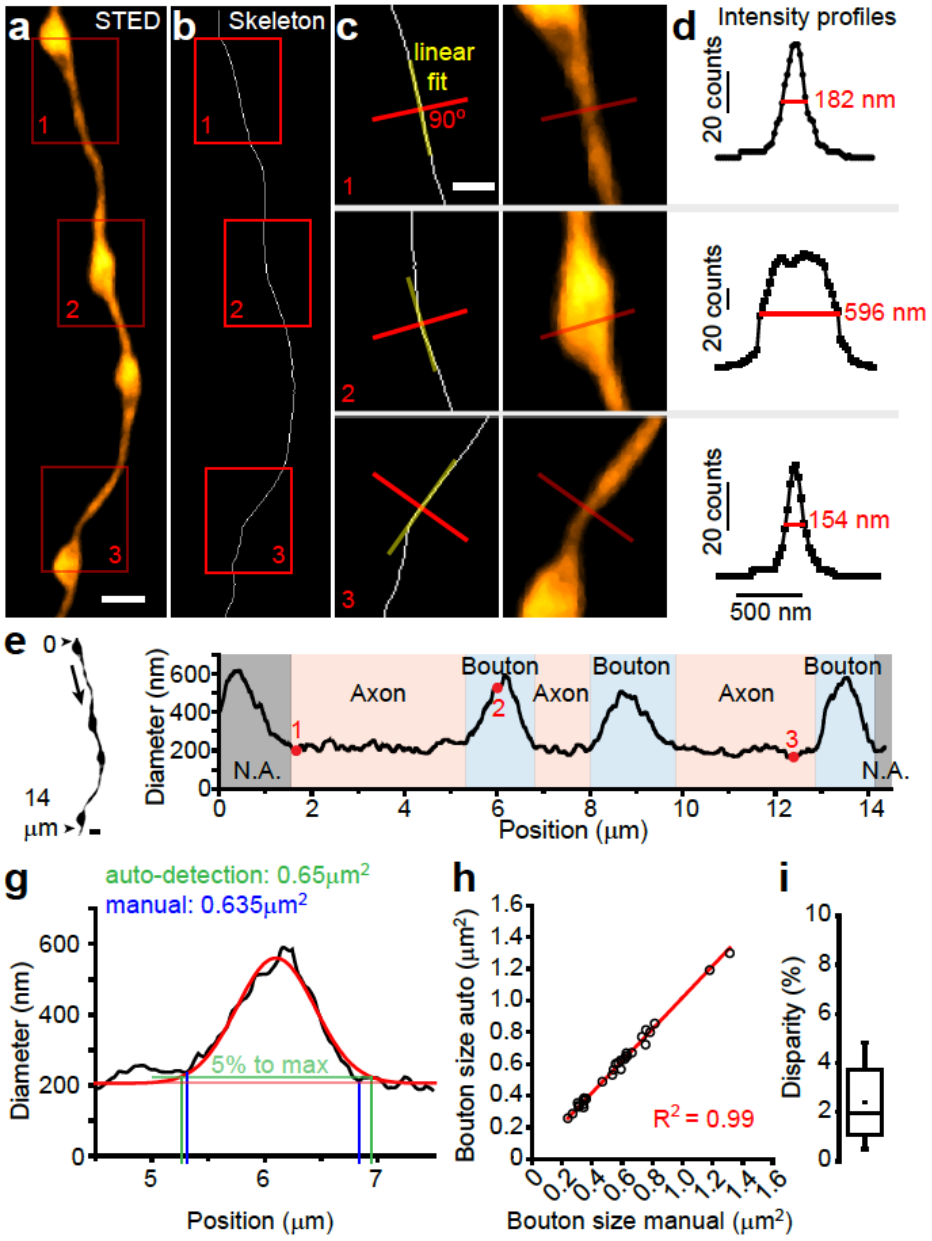

Fig. S2. Analysis of axonal morphology

a, The morphology was measured on the maximum intensity projection of a z-stack series of isolated axonal stretches as shown in this example. **b,** From this image, a skeleton image, consisting of a line of pixels that follows the axon path, was automatically generated and used as a reference for the measurement. **c,** For every pixel along the line, a local linear fit was calculated using 30 neighboring pixels (yellow lines on the 3 example regions from b). The orthogonal line (red line) was used to collect the STED image pixel intensity profiles. **d,** From the raw intensity profiles, the full width half maximum, reflecting the structure diameter, was automatically calculated for each pixel position. **e,** Diameter profile of the axon stretch analyzed (left schematic shows the direction of the measurement; red dots show the measurements from the 3 regions of interest). The selection of boutons and axon shaft segments were visually determined based on the diameter profile (red: axon segment; blue: bouton; N.A.: incomplete structures not analyzed. **g-i,** Validating manual with automated detection of bouton edges. **g,** Diameter profile of a bouton (black trace) and fitted with a Gaussian function (red trace). The automated detection of edges was determined as the width at the 5% maximum of the Gaussian fit (horizontal green line). The automated detection of edges is shown in green and manual detection is shown in blue. **h,** Comparison between bouton size based on manual vs. automated edge detection (R^2=0.99 for the equation $x_{manual}=y_{auto}$, n=30 boutons). **i,** Disparity in bouton size measurement between manual vs. automated edge detection methods calculated as: $|Size_{auto} - Size_{manual}| / Size_{manual}$ (2.4 ± 1.3% mean ± SD). Scale bars, 1 µm (a, e), 0.5 µm (c).

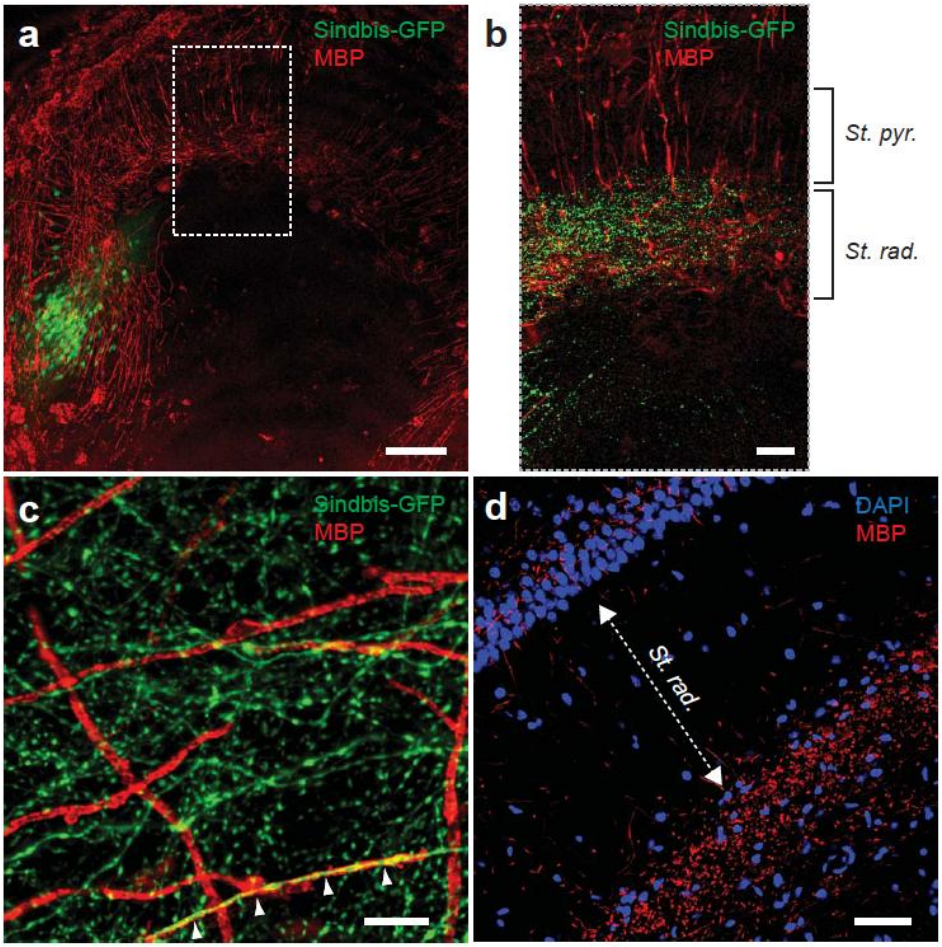

Fig. S3. The vast majority of CA3 axons are unmyelinated

a, Myelin immunostaining on a 5 weeks old organotypic hippocampal slice with GFP-labelled CA3 neurons. **b**, CA1 region magnified with enhanced contrast showing a high density of CA3 axons (green) in the *stratum radiatum*. **c**, High resolution image of MIP (z-stack = 4 µm) in the CA1 *stratum radiatum* shows that the vast majority of CA3 axons are unmyelinated. Anecdotally, a segment exhibited myelin (indicated by white arrows). **d**, Fixed brain slice showing a similar low density of myelination in the CA1 *stratum radiatum* suggesting that CA3 axons are largely unmyelinated in adult mice. Scale bars, 200 µm and 50 µm (a), 10 µm (c and d).

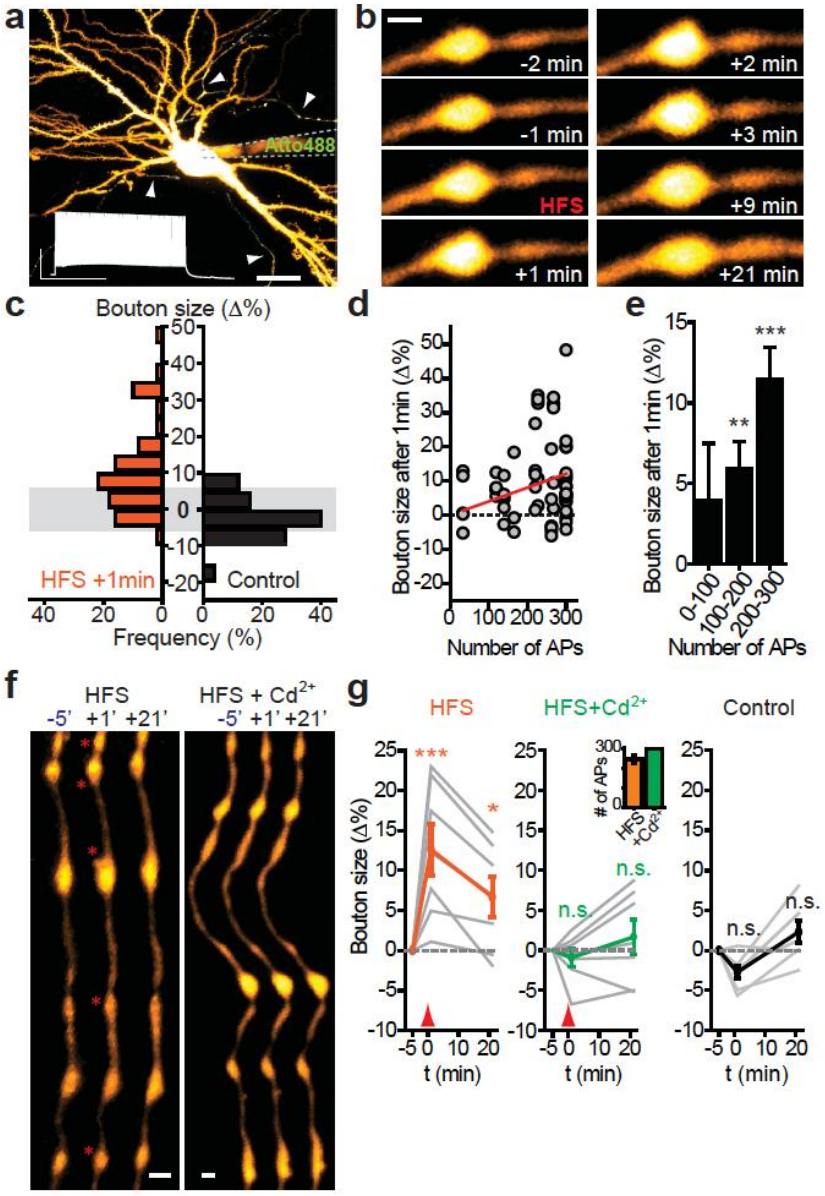

Fig. S4. Single-cell approach confirms activity-dependent enlargement of synaptic boutons

a, Single-cell axon labelling with Atto488 (white arrows indicate the axon) and high frequency train of APs triggered by current injection at the soma (scale bars; 50 mV and 0.5 sec). **b**, Time lapse imaging shows transient enlargement of a synaptic bouton immediately after HFS. **c**, Frequency distribution of bouton size change 1 min after HFS compared to non-stimulated control conditions (HFS, n = 50 boutons from 7 cells with stimulation ≥ 200 APs, from 5 slices; Control, n = 24 boutons from 7 cells, from 4 slices). **d**, Individual bouton size change 1 min after HFS as a function of number of APs generated at the soma during the stimulation protocol (n = 62 boutons from 11 cells, 8 slices, $R^2 = 0.4$). **e**, Same data binned showing the magnitude of bouton change increases with the number of APs generated during the stimulation (one-sample Wilcoxon test of the mean different from 0: 0-100, n = 5 boutons, P > 0.3; 100-200, n = 14, P < 0.01; 200-300, n = 43, P < 0.001, from 8 slices). **f**, Bouton size increase is prevented by 100 µM of cadmium applied to the bath solution 10 min prior to the HFS (asterisks indicate boutons that underwent a transient size increase). **g**, Time course of bouton size show a significant increase of bouton size immediately after HFS (one-way repeated ANOVA and Dunnett's tests; n = 7 cells from 5 slices, with stimulation > 200 APs, +1 min vs. before, 12.6 ± 3.2%, P < 0.001, +21 min vs. before, +6.7 ± 2.5%, P < 0.05) while it is blocked by cadmium (Cd^{2+}; n = 7 cells from 4 slices, with stimulation > 200 APs, +1 min vs. before, -0.9 ± 1.1%, P > 0.7, +21 min vs. before, +1.7 ± 2.2%, P > 0.4) and stable in control conditions (Control: n = 7 cells from 6 slices, +1 min vs. before, -2.7 ± 0.8%, P > 0.07, +21 min vs. before, +2.3 ± 1.4%, P > 0.13). The inset shows the average number of APs delivered during the stimulation indicating that cadmium does not affect spiking (HFS: 249 ± 22 / 300 APs; $+Cd^{2+}$: 300 / 300 APs on average). Data displayed as mean ± s.e.m. n.s., not significant; *P < 0.05; **P < 0.01; ***P < 0.001. Scale bars, 20 µm (a), 1 µm (b and f).

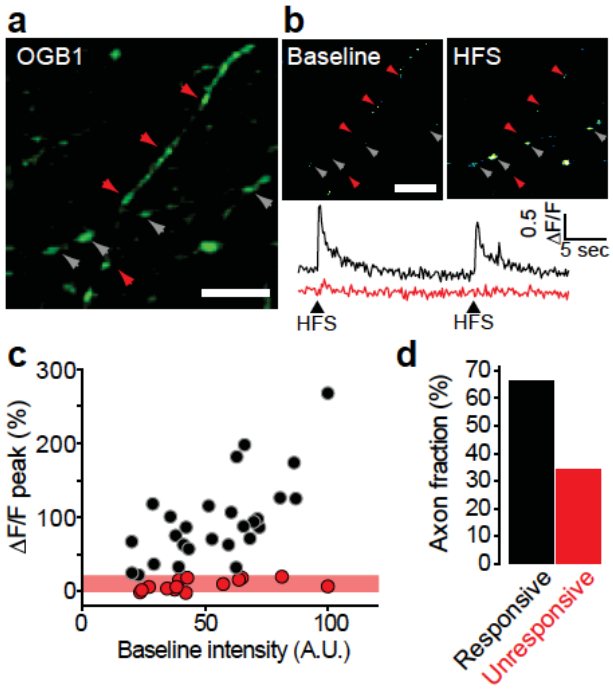

Fig. S5. Electrical stimulation of imaged axon fibers

a, Z-projection of CA3 axons loaded with Oregon Green 488 BAPTA-1 (OGB-1 AM) imaged in the CA1 *stratum radiatum*. Two distinct axon segments are identified in the image (indicated by red and grey arrows). **b**, One of the segments responds to electrical HFS (grey arrows and black trace) whereas the other one did not (red arrows and trace). **c**, The peak values of ΔF/F plotted against the baseline intensity of the axon segment, showing that detection of Ca^{2+} responses did not depend on baseline fluorescence intensity (failure was defined as peak ΔF/F < 20%, marked with red points; n = 41 axon segments analyzed, 2 slices). **d**, 34 % of the segments did not show any Ca^{2+} responses during HFS (n = 41 axon segments analyzed, 2 slices). Scale bars: 5 µm.

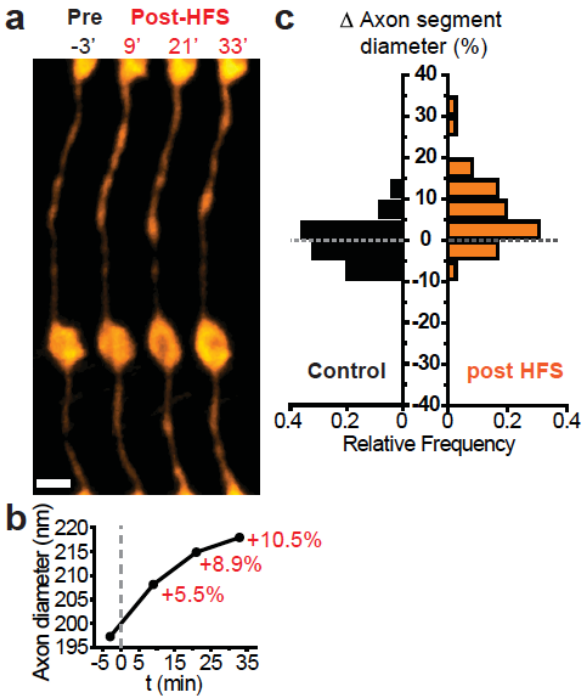

Fig. S6. Distribution of axon diameter changes

A substantial fraction of axon segments exhibited increases in diameter greater than 10%. **a**, Example of an axon segment becoming wider after HFS. **b**, Average axon diameter of the segment shown in panel **a** revealed a 10.5% increase after 33 min. **c**, Distribution of the changes in axon segment diameter after HFS compared to control conditions (all experiments pooled, control; n = 41 segments; HFS; n = 28 segments). Scale bar: 1 µm.

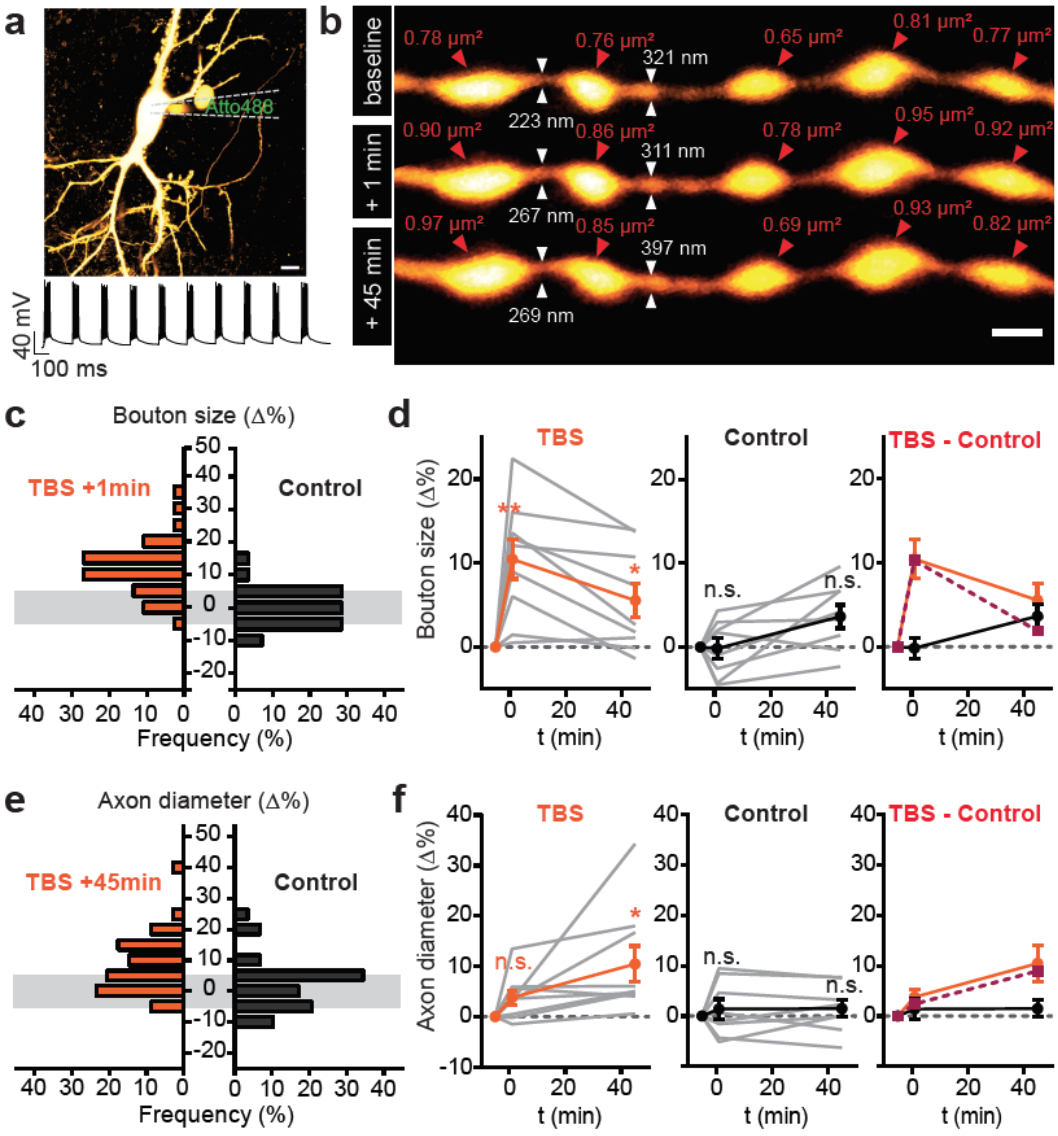

Fig. S7. Bouton and axon enlargement induced by TBS

a, Single-cell axon labeled with Atto488 under theta burst stimulation (top) and theta-burst train of APs triggered by current injection at the soma (bottom). **b,** Rapid enlargement of synaptic boutons and a late change in the diameter of the axon shaft after TBS were observed by time lapse STED imaging (red arrows indicate bouton size, white arrows indicate axon diameter). **c,** Frequency distribution of individual bouton size change 1 min after TBS compared to non-stimulated control conditions (HFS, n = 37 boutons from 9 cells, 9 slices; Control, n = 28 boutons from 8 cells, 8 slices). **d,** Time course of normalized bouton size show a significant increase of bouton size immediately after TBS (one-way repeated ANOVA and Dunnett's tests; n = 9 cells from 9 slices, +1 min vs. before, +10.45 ± 2.34%, $P < 0.01$, +45 min vs. before, +5.53 ± 2.01%, $P < 0.05$) and in control (n = 8 cells from 8 slices, +1 min vs. before, -0.42 ± 1.34%, $P > 0.9$, +45 min vs. before, +3.65 ± 1.41%, $P > 0.06$). **e,** Frequency distribution of individual axon diameter change 45 min after TBS compared to non-stimulated control conditions (HFS, n = 34 individual 1 µm-long segment from 9 cells, 9 slices; control, n = 29 individual 1 µm-long segment from 8

cells, 8 slices). **f,** Time course of normalized axon diameters show a significant increase of shaft diameter immediately after TBS (one-way repeated ANOVA and Dunnett's tests; n = 9 cells from 9 slices, +1 min vs. before, +3.75 ± 1.48%, P > 0.06, +45 min vs. before, +10.39 ± 3.58%, P < 0.05), but not in control (n = 8 cells from 8 slices, +1 min vs. before, +1.38 ± 1.97%, P > 0.7, +45 min vs. before, +1.45 ± 1.67%, P > 0.6). The graphs on the right side of panel (**d**) and (**f**) show the time course of TBS-induced morphological changes corrected for the slight run-up in the morphological parameters during control conditions (TBS-Control; dotted red line). Data displayed as mean ± s.e.m. n.s., not significant; *P < 0.05; **P < 0.01. Scale bars, 10 µm (a), 1 µm (b).

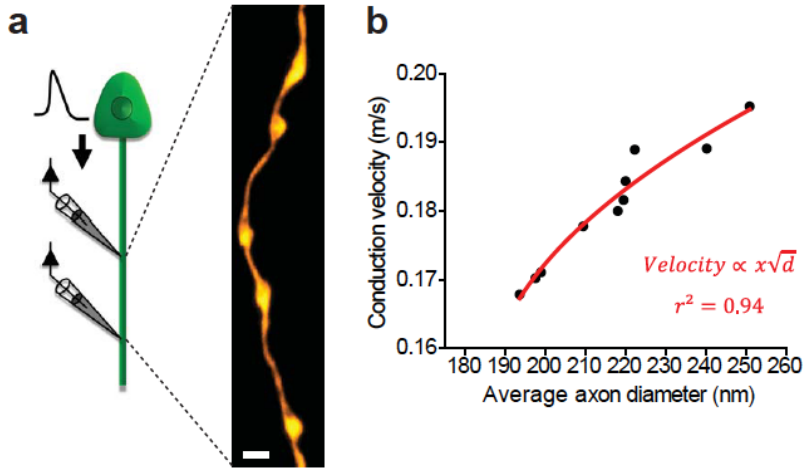

Fig. S8. Square-root dependence of AP velocity on axon diameter

a, The simulation of AP conduction velocity was based on STED morphological data of axon segments. **b**, The relationship between measured conduction velocity and mean diameters of axon segments follows a square-root function ($R^2 = 0.94$) as predicted by basic biophysical theory. Scale bar: 1 µm.

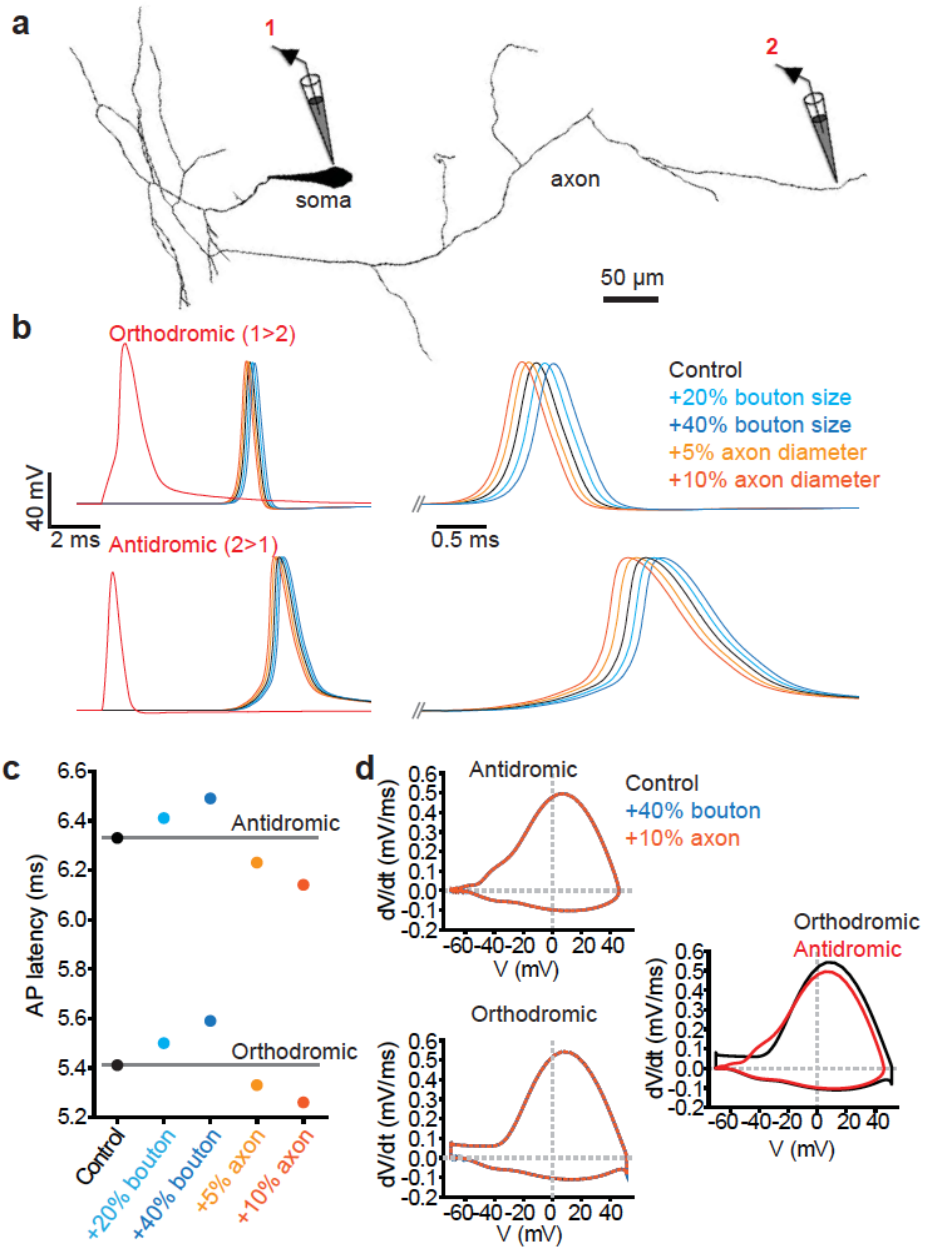

Fig. S9. Differences between orthodromic and antidromic AP propagation

a, A reconstruction of a proximal CA3 axon arbor based on the STED data was used to simulate the effects of morphological changes on orthodromic and antidromic AP propagation. **b**, Simulated propagation of an AP generated at the soma (electrode 1, shown in panel **a**) and reaching the end of the axon (electrode 2) (top traces), or generated at the axon and propagating back to the soma (bottom traces). In both cases, enlarging boutons delays conduction, whereas increasing the axon diameter boosts conduction velocity (right). **c**, AP latency shows that antidromic conduction is slower but the relative changes after morphological changes are similar. **d**, Phase plot analysis showing that morphological changes in axons or boutons do not appreciably affect AP waveform. However AP waveforms of orthodromic and antidromic propagation are different.

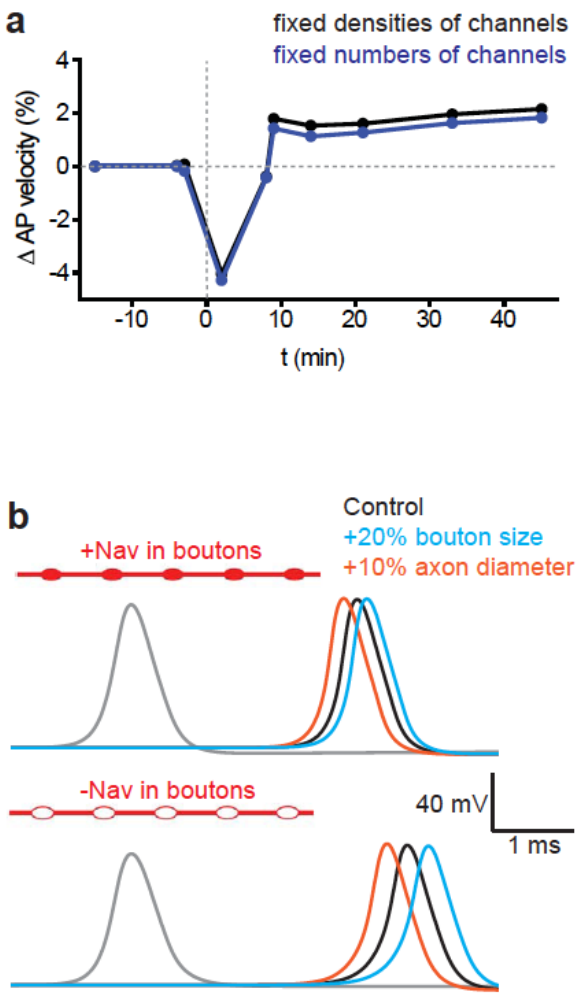

Fig. S10. Effect of channel density and number

a, Simulations based on the time course and magnitude of the experimentally observed morphological changes with the constraint that either the density (black trace) or the total number (blue trace) of the voltage-gated channels ($Na^+/K^+/Ca^{2+}$) in the axonal membrane are kept constant. Both conditions produced very similar results. **b**, Simulations of an AP propagating through 0.5 mm axon segment exhibiting boutons every 3 µm (grey traces, AP at the start; colored traces, AP at the end of the segment) with boutons containing Na_v channels (Na_v; top) and without (bottom). When Na_v channels were absent from boutons, AP amplitude was reduced, AP duration was increased and AP conduction velocity decreased. At the same time, the effects of the morphological changes on AP velocity (bouton size increase, blue; axon diameter enlargement, orange) were enhanced.

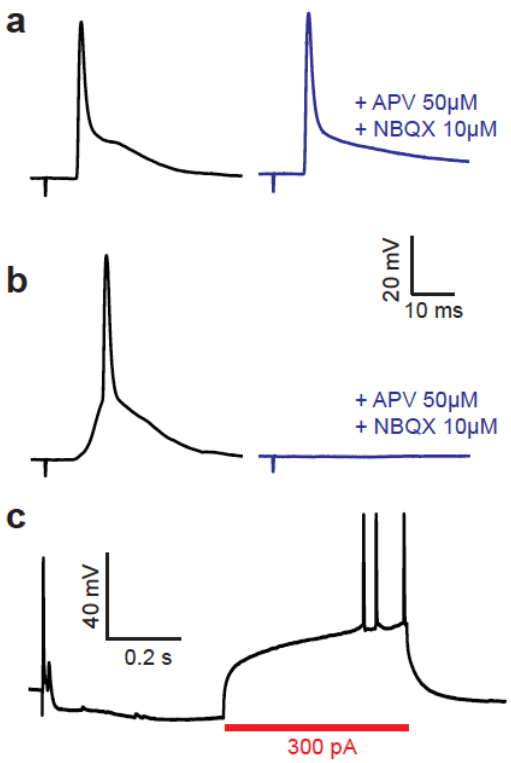

Fig. S11. Electrophysiological responses due to direct or synaptically-mediated stimulation

a, Responses from direct axonal stimulation showed a sharp rising phase reflecting the depolarization of the AP followed by a small depolarization from EPSPs. **b**, By contrast, synaptically-mediated APs showed an initial slow rising phase corresponding to synaptic EPSPs followed by the fast rising phase of the AP when the potential reaches threshold. APV and NBQX blocked the synaptically evoked responses, but not the AP induced by direct axonal stimulation. **c**, Recording of an antidromic AP followed by somatically evoked APs. The difference in amplitude indicates that antidromic APs are not actively propagated in the soma, resulting in voltage attenuation.

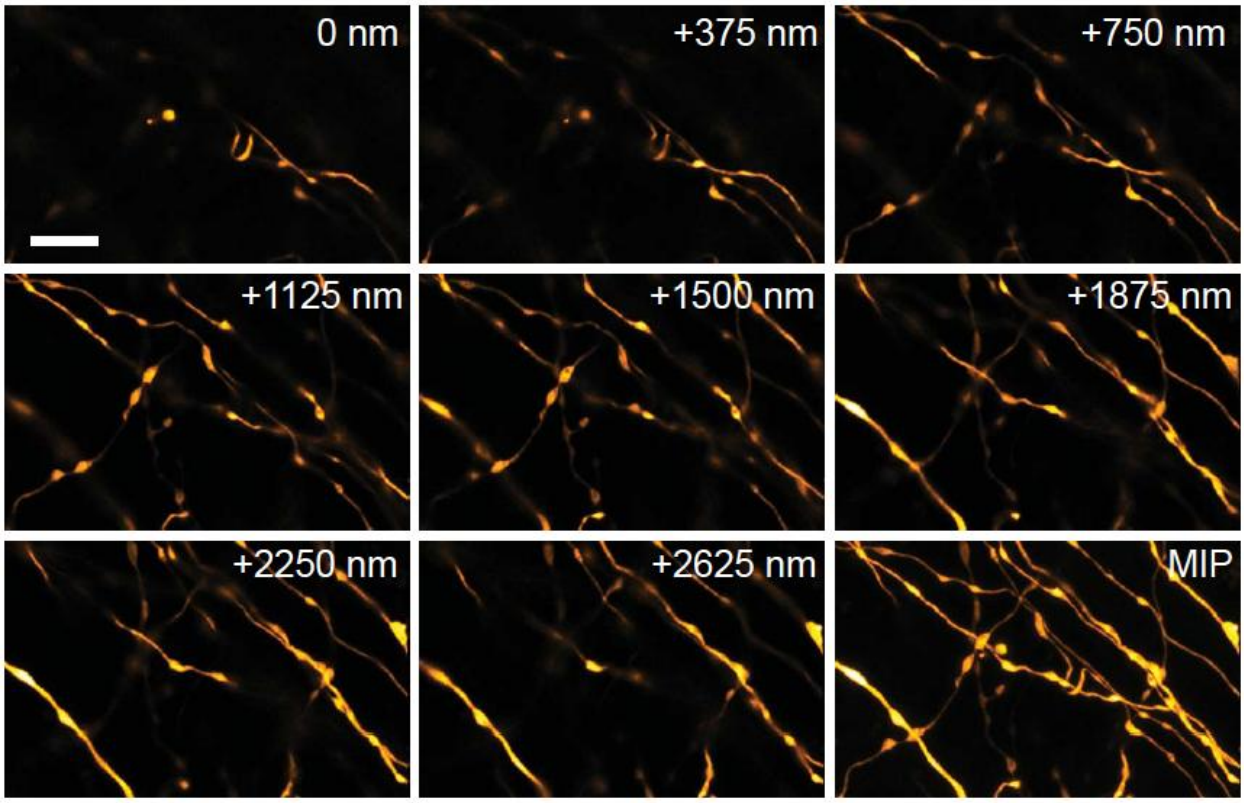

Fig. S12. Raw STED image stack

Z-series of single image sections that underlie the maximum intensity projection shown in Fig. 1c (8 sections with a Δz of 375 nm). Scale bar, 5 µm.

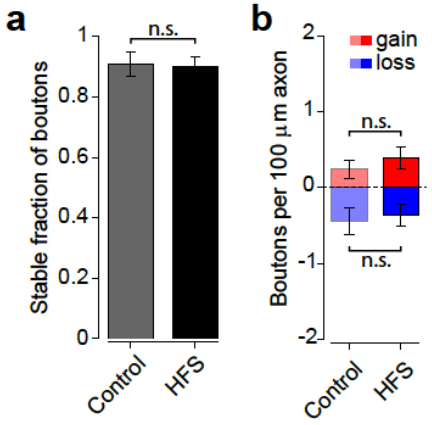

Fig. S13. Gain and loss of boutons after HFS

a, Fraction of boutons that are stable in control (grey bar) and HFS (black bar) experiments are not significantly different (two-sample t-test, P = 0.92, n = 8 slices in both control and HFS groups for a total axon length analyzed of 486 µm in control group 389 µm in HFS group). **b,** Summary of the bouton turnover in control and after HFS (bouton gained in red; bouton loss in blue). The gained and lost fractions after HFS were not significantly different from control conditions (two-sample t-test, gain. P = 0.46; loss: P = 0.72). Data displayed as mean ± s.e.m., n.s., not significant.